Nanoscale

PAPER

View Article Online
View Journal | View Issue

Cite this: *Nanoscale*, 2017, **9**, 18723

Tomographic magnetic particle imaging of cancer targeted nanoparticles†

Hamed Arami,[a,b] Eric Teeman,[a] Alyssa Troksa,[a] Haydin Bradshaw,[c] Katayoun Saatchi,[d] Asahi Tomitaka,[e] Sanjiv Sam Gambhir,[b,f] Urs O. Häfeli,[d] Denny Liggitt[g] and Kannan M. Krishnan*[a]

Magnetic Particle Imaging (MPI) is an emerging, whole body biomedical imaging technique, with sub-millimeter spatial resolution and high sensitivity to a biocompatible contrast agent consisting of an iron oxide nanoparticle core and a biofunctionalized shell. Successful application of MPI for imaging of cancer depends on the nanoparticles (NPs) accumulating at tumors at sufficient levels relative to other sites. NPs' physiochemical properties such as size, crystallographic structure and uniformity, surface coating, stability, blood circulation time and magnetization determine the efficacy of their tumor accumulation and MPI signal generation. Here, we address these criteria by presenting strategies for the synthesis and surface functionalization of efficient MPI tracers, that can target a typical murine brain cancer model and generate three dimensional images of these tumors with very high signal-to-noise ratios (SNR). Our results showed high contrast agent sensitivities that enabled us to detect 1.1 ng of iron (SNR ~ 3.9) and enhance the spatial resolution to about 600 μm. The biodistribution of these NPs was also studied using near-infrared fluorescence (NIRF) and single-photon emission computed tomography (SPECT) imaging. NPs were mainly accumulated in the liver and spleen and did not show any renal clearance. This first pre-clinical study of cancer targeted NPs imaged using a tomographic MPI system in an animal model paves the way to explore new nanomedicine strategies for cancer diagnosis and therapy, using clinically safe magnetic iron oxide nanoparticles and MPI.

Received 27th July 2017,
Accepted 19th October 2017

DOI: 10.1039/c7nr05502a

rsc.li/nanoscale

Introduction

Magnetic Particle Imaging (MPI) is a novel biomedical imaging technique, incorporating high contrast agent mass sensitivity (~5 nanograms Fe per μL (ref. 1)), and sub-mm spatial resolution,[2] that is linearly quantitative with NP concentration, and with zero tissue depth signal attenuation.[3–6] Furthermore, MPI involves no ionizing radiation and uses bio-compatible superparamagnetic iron oxide nanoparticles (NPs) as contrast agents thereby enhancing its clinical safety.[7–9] These unique advantages of MPI offer promise in a wide range of clinical applications such as cardiovascular imaging, cancer diagnosis, brain injury detection, lung perfusion imaging, and *in vivo* tracking of magnetically labeled stem cells.[10–15] However, efforts to improve MPI scanners/spectrometers and design of functionalized contrast agents are still required to not only enhance MPI performance such as spatial resolution, signal intensity and imaging speed, but also to develop promising translational medical applications.[16]

Here, we study the cancer targeting ability of our functionalized MPI contrast agents in mice with brain cancer xenografts, and assess MPI capabilities for targeted and tomographic imaging of cancer. To enhance specific tumor targeting, we conjugated lactoferrin (a brain cancer targeting peptide[17]) to the NPs and used an external magnet to improve the localization of the NPs to tumor xenografts. Using MPI, we were able to visualize only nanoparticles that were embedded in tissues, based on their intrinsic magnetic responses. Therefore, unlike MRI, we did not see background interference from surrounding diamagnetic tissues and the signals were depth-independent, as generally expected in MPI. We have also developed a

[a]Department of Materials Science, University of Washington, Seattle, Washington, 98195, USA. E-mail: kannanmk@uw.edu
[b]Department of Radiology, Molecular Imaging Program at Stanford, Stanford School of Medicine, Stanford, California, 94305, USA
[c]Department of Chemistry, University of Washington, Seattle, Washington, 98195, USA
[d]Faculty of Pharmaceutical Sciences, University of British Columbia, Vancouver, Canada
[e]Department of Immunology, Herbert Wertheim College of Medicine, Florida International University, Miami, USA
[f]Departments of Bioengineering & Materials Science & Engineering, Stanford University, Stanford, California, 94305, USA
[g]Department of Comparative Medicine, University of Washington School of Medicine, Seattle, Washington, 98195, USA

†Electronic supplementary information (ESI) available. See DOI: 10.1039/c7nr05502a

generalized platform for functionalization of individual NPs for multimodal imaging, combining MPI, near-infrared fluorescence (NIRF) imaging, single-photon emission computed tomography (SPECT) and computed tomography (CT) modalities, in order to study the biodistribution of these NPs in mice more accurately. Such critical proof-of-concept studies provide the necessary information for future applications of MPI with optimized contrast agents for tomographic and quantitative cancer imaging and diagnosis, in combination with other imaging modalities such as fluorescence imaging, SPECT/PET and magnetic resonance imaging (MRI).

Results and discussion

The signal in MPI originates directly from the superparamagnetic iron oxide nanoparticles and is proportional to the field dependent magnetization response of the NPs ($\chi_{diff} = dm/dH$, where $m = M_s V$, is the magnetic moment of individual NPs of volume, V and saturation magnetization, M_s, and H is the applied field in a typical MPI scanner).[18] In the *x*-space MPI image reconstruction method, improvements in image quality can be represented by narrower full width at half maximum (FWHM) and larger peak heights of nanoparticles dm/dH, measured by using a magnetic particle spectrometer (MPS).[6,19–21] Here, we use thermodynamically phase-pure and monodisperse nanoparticles ($d_C \sim 25$–27 nm), with near ideal saturation magnetization,[22] and long blood circulation times,[11] optimized for cancer diagnosis using MPI (Fig. 1 and S3†). This is critical for cancer targeted MPI, since phase pure NPs in this size range generate much higher MPI signal intensities, which enables imaging of the tumors with higher sensitivities (per unit mass of the NPs) using MPI, when only a small fraction (*i.e.*, nanograms) of the administered NPs accumulate in tumors.

Details of our core synthesis procedure and structural parameters are reported elsewhere.[22–24] Incomplete oxidation of the iron oxide nanoparticles leads to the presence of Wüstite (FeO), an antiferromagnetic phase, in NPs which results in dramatic deterioration in their MPS and MPI performance, as shown by an increase in the FWHM (*i.e.*, loss of resolution in MPI, Fig. S3a†). Controlled oxidation to obtain pure magnetite NPs results in a very narrow dm/dH peak, with a FWHM of about 60% of commercial Resovist™ iron oxide NPs. Note that the hydrodynamic size and polydispersity index of the NPs measured by the DLS method were almost identical ($d_H \sim 55$–65 nm, PDI ~ 0.2–0.25). Such variations in the MPS dm/dH response were also reflected in the near-zero field derivatives of dc *m*–*H* measurements of these two types of NPs (Fig. S3b†). In spite of their similar sizes observed in TEM, single crystalline phase-pure magnetite NPs were rapidly magnetized and reached their saturation magnetization at much smaller field values, compared to FeO/Fe_3O_4 heterogeneous structures, a phenomenon which resulted in their significantly improved MPI performance (*i.e.*, narrower FWHM of the point spread function, or PSF, in MPS). The phase purity and tuned size of the NPs enhanced their detection sensitivity and achievable spatial resolution. Our *in vitro* results (Fig. S4a†) showed that we were able to detect about 1 ng of these NPs (total volume 2–3 μL, SNR = 3.9). A larger volume of the NPs (~200 μL) with a concentration of ~550 pg Fe per μL could be feasibly imaged (SNR = 4.9) using our scanner (Fig. S4b†). The signal intensity changes linearly with the concentration of the NPs, ranging from less than 10 ng Fe per μL to about 10 000 ng Fe per μL (Fig. S4c†), which is critical for quantitative imaging of NPs in tissues and cells. Finally, we were able to distinguish the NP solutions (1–2 μL each) placed at different distances (~4600, 1400 and 600 μm) relative to each other, showing a high spatial resolution of less than 600 μm (Fig. S5†) with our optimized contrast agents and a preclinical MPI scanner (Magnetic Insight, Momentum).

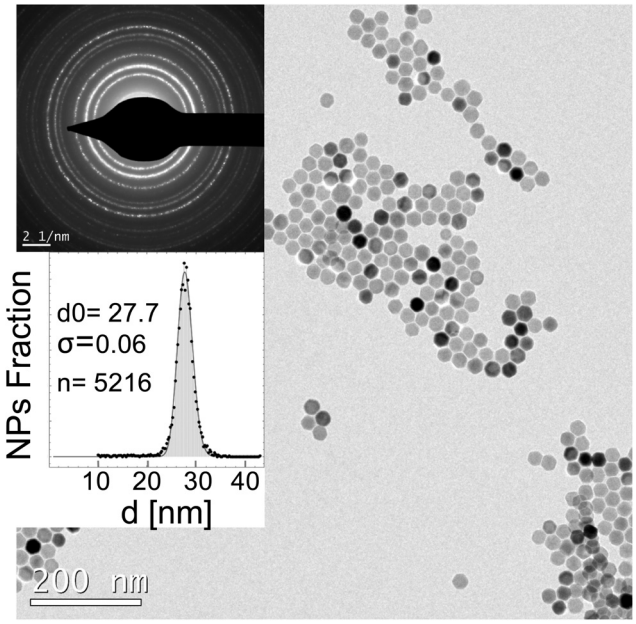

Fig. 1 Synthesis of highly monodisperse and superparamagnetic nanoparticles with near-theoretical possible magnetic susceptibility optimized for MPI. The TEM image (scale bar: 200 nm), electron diffraction pattern (scale bar: 2 1/nm), and size distribution histogram of the optimized phase pure NPs synthesized by thermal decomposition of iron oleate in the presence of an oleic acid surfactant, followed by their controlled oxidation in the presence of oxygen.

NPs were coated with PMAO-PEG co-polymer molecules, in which PEG molecules were functionalized with a maleimide group (Fig. 2a and b). Maleimides are highly reactive with thiols (–SH), which makes them a suitable platform for the conjugation of various types of targeting peptides to thiol groups on their backbone structure. We used lactoferrin, since our recent *in vitro* studies have shown that they can effectively target C6 brain cancer cells, presenting a reasonable MPI signal after cellular internalization.[17] Since lactoferrin lacks any thiol groups, but has a large number of amine groups on its backbone structure, we transformed some of these amine groups to thiols with the help of Traut's reagent (Fig. 2c).[25]

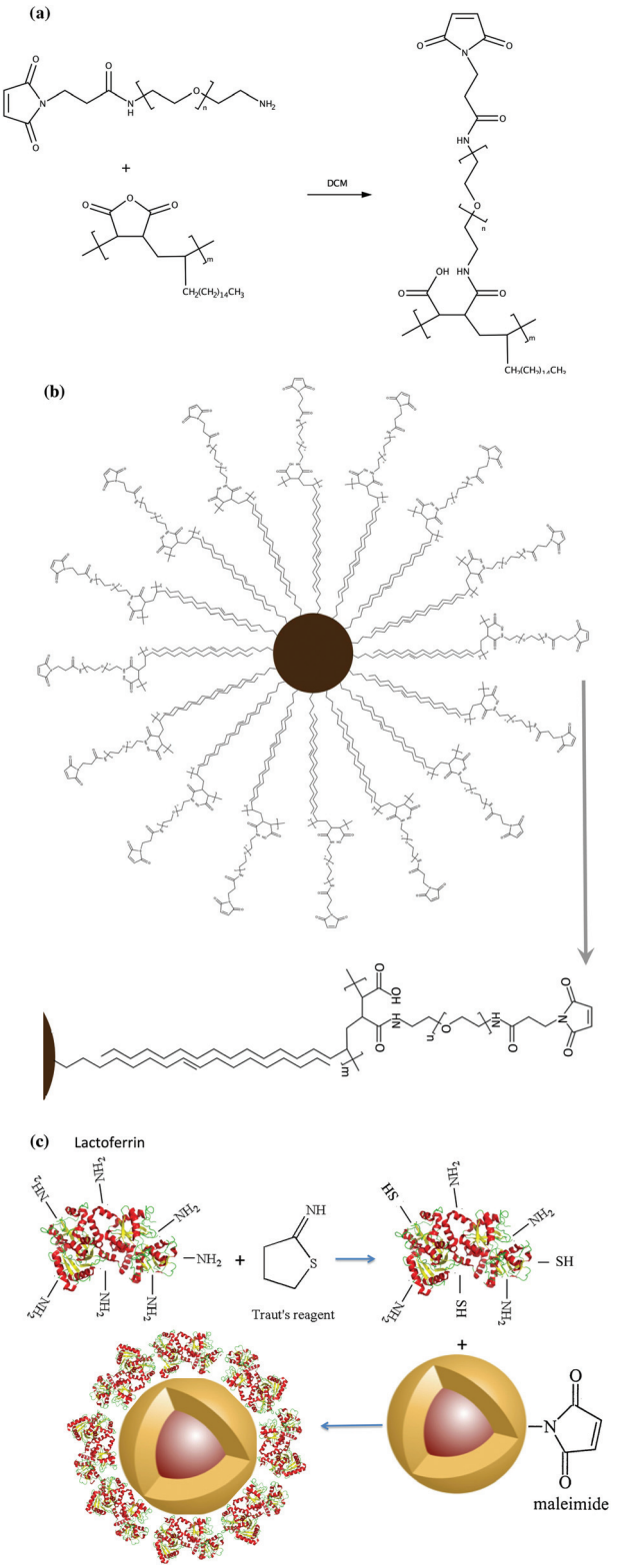

Fig. 2 Schematics showing surface functionalization of the optimized MPI contrast agents for glioma targeting. (a) Synthesis of the PMAO-PEG co-polymer, with active maleimide functional groups and (b) its assembly on the surface of the oleic acid coated nanoparticles after phase transfer to aqueous phases. (c) Thiolation of the lactoferrin molecules using Traut's reagent and their conjugation to maleimide functionalized MPI contrast agents for *in vivo* brain cancer targeting experiments.

The thiolated lactoferrin was then conjugated to maleimide groups of the PMAO-PEG coating molecules on the surface of the NPs (Fig. 2c). Cy5.5-NHS NIRF molecules were also conjugated to the lactoferrin molecules using methods we reported earlier.[17,26] NPs without lactoferrin on their surface were used as control samples to evaluate the role of lactoferrin in tumor uptake. Dynamic light scattering (DLS) measurements showed that the hydrodynamic sizes of the conjugated lactoferrin and control NPs were 112 and 104 nm, respectively.

The evaluation of the NP uptake in tumors, 1 and 2 hours after tail-vein injection, was carried out using a MPI scanner and a near-infrared fluorescence imaging system (IVIS); the magnetic and fluorescence signals of the excised tumors were also measured by using the IVIS, an MPS (frequency ~25 kHz) and a MPI scanner. The tissue fluorescence signal intensity is highly dependent on the number of fluorescent-tagged nanoparticles accumulated within them as MPS and MPI signals are quantitative and depend linearly on the concentration of the magnetic nanoparticles. MPS is an accurate and quick representative technique to evaluate the MPI signal of the tissues (similar to nuclear magnetic resonance or NMR *versus* MRI). Mice were divided into four different groups and injected with: (1) lactoferrin-conjugated NPs combined with an external magnet to enhance the targeting, (2) lactoferrin without an external magnet, (3) NPs without lactoferrin on their surface to evaluate enhanced permeation and retention (EPR) mediated accumulation, and (4) phosphate buffered saline (PBS) as a control.

Overall, our *in vivo* (Fig. 3, 4 and S6–S10†) and *ex vivo* results (Fig. 5) showed that nanoparticles accumulated within the tumors based on three mechanisms: (1) the EPR effect, associated with the passive diffusion of particles through the presumably leaky vasculature (enhanced permeation) and subsequent accumulation in the tumors (retention); (2) ligand (lactoferrin) assisted accumulation and (3) external magnetic targeting. Generally, these three mechanisms depend on the nanoparticle blood circulation time, hydrodynamic size, surface coating and charge (zeta potential).[27] Whole body NIRF and MPI images showed a much lower uptake in the tumors due to the EPR effect (Fig. 3c, S7c and S10†); however, the lactoferrin conjugated NPs were readily internalized and retained in xenografts (Fig. 3b, S7b and S9†), and uptake was enhanced when we placed a magnet adjacent to the tumors (Fig. 3a, d, S7a and S8†). Tomographic analyses of the MPI results enabled us to determine the 3D distribution of the NPs in tumors and livers (Fig. 4d and ESI Videos 1–3†). Note that the color scale bar ranges of these videos are the same as their counterpart 2D images shown in Fig. 4. The MPI results and NIRF images of the excised tumors (Fig. 4, 5a and ESI Videos 1–3†) showed that the tumor uptake, based on these mechanisms is cumulative, with the combination of magnetic and lactoferrin-assisted targeting showing the greatest uptake. These results were also confirmed by MPI signal analyses of the tumor tissues from the excised xenografts (Fig. 5b).

Exploiting the versatility of our surface functionalization platform, we also radiolabeled our optimized nanoparticles for

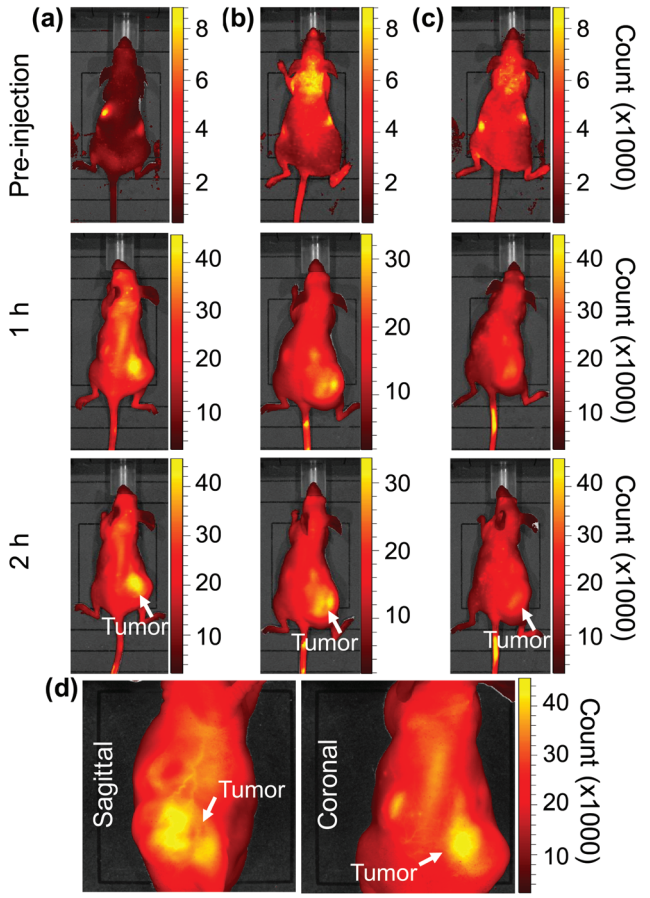

Fig. 3 Near-infrared fluorescence (NIRF) images of the tumor xenografts. Images of the mice injected with Cy5.5–lactoferrin conjugated NPs, with (a) and without (b) a permanent magnet placed adjacent to the tumor xenograft on the right side flank, compared with mice injected with Cy5.5-labeled NPs, without using lactoferrin and magnetic targeting (c). (d) Higher magnification sagittal and coronal images of the tumors, 2 h after magnetic targeting. Three mice were used for each condition and pre-injection and post-injection (1 and 2 h) images were captured from four different mice positions to show NPs' accumulation in tumors clearly (see additional mouse images in Fig. S4–S8†).

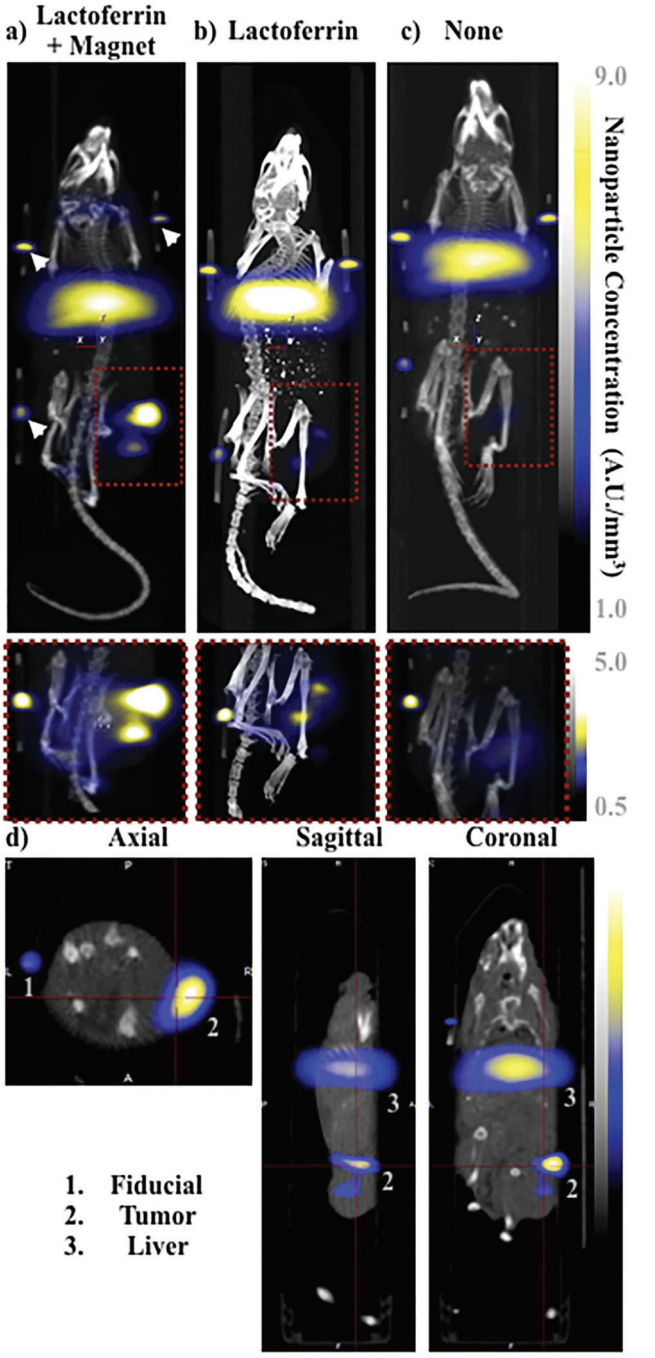

Fig. 4 MPI images of the mice with tumor xenografts. Two-dimensional (2D) MPI/CT images (2 h post-injection) of mice injected with Cy5.5–lactoferrin conjugated NPs, with (a) and without (b) a permanent magnet placed adjacent to the tumor xenograft on the right side flank, compared with the mice injected with Cy5.5-labeled NPs, without using lactoferrin and magnetic targeting (c). The tumors are marked with the red squares. Rescaled images are shown below each mouse to highlight the tumors. Three fiducial points (white arrowheads in (a)) were used for registration of the MPI and CT images. Also see ESI Videos 1–3,† showing the three dimensional tumor images. Axial, sagittal and coronal images of the tumors of the mice (a) are shown in (d). The liver can also be seen in the sagittal and coronal images.

SPECT/CT contrast imaging, using ^{67}Ga-NOTA and forming a thiourea bond with amine groups present on the surface of the nanoparticles (Fig. S1†). The abundant number of amine groups on the surface of the nanoparticles made them suitable platforms for radiolabeling with ^{67}Ga-NOTA. This molecule has an isothiocyanate group that can feasibly react with amine groups on the surface of the NPs by forming a thiourea bond.[28] The NOTA molecules did not get separated after storage for 2–3 days or during the purification and thin-layer chromatography (TLC) analyses of the radiolabelled NPs, which further confirms the formation and stability of this covalent bond. SPECT imaging provided high tracer mass sensitivity, enabling accurate, quantitative estimation of NP concentration in the major clearance organs (*i.e.*, liver, spleen and kidneys) and other tissues.[29] SPECT/CT imaging (Fig. S11 and ESI Videos 4 and 5†) and biodistribution studies (Fig. S12†) confirmed that NPs only accumulated in the liver and spleen

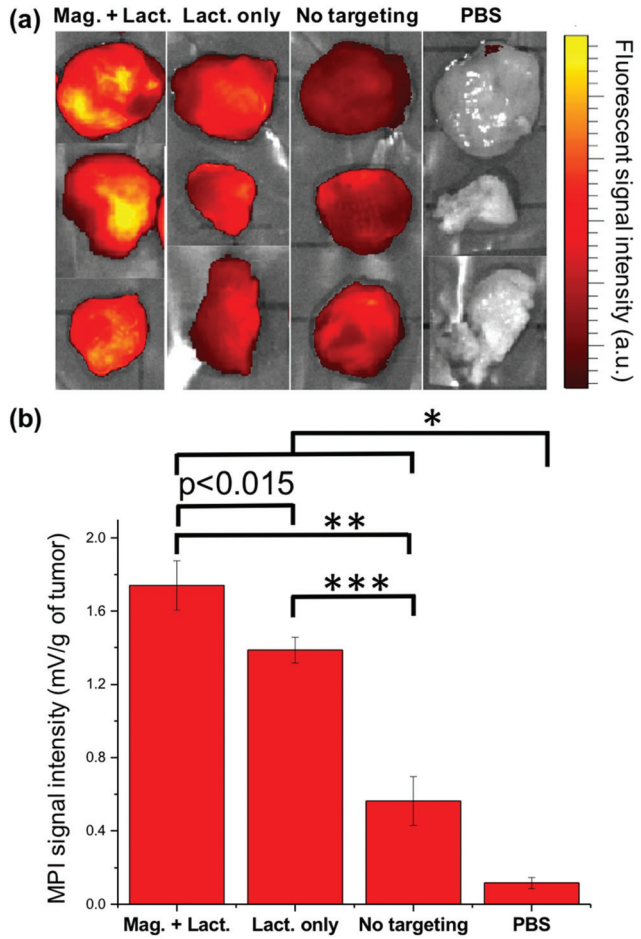

Fig. 5 *Ex vivo* evaluation of the uptake of MPI contrast agents by tumor xenografts. (a) NIRF images and (b) representative MPI signal intensities (per tumor mass) of the tumor xenografts excised from mice (mean ± standard deviation; n = 3) injected with Cy5.5–lactoferrin conjugated NPs, with (Mag. + Lact.) and without (Lact. only) using magnetic targeting, compared with Cy5.5-labeled NPs (without any lactoferrin and magnetic targeting) and PBS as controls. Signal intensities were measured using a magnetic particle spectrometer. Significance was confirmed by one-way ANOVA with Bonferroni's multiple comparison correction *p < 0.05, **p < 0.0005 and ***p < 0.0001. In NIRF images brightness is proportional to the uptake of the fluorescently labeled NPs, while in MPI measurements, bars represent the MPI signal intensity (dm/dH) only generated from a magnetic response of the NPs without any background signal from the tissues.

4 h after injection, with almost no traces of NPs in kidneys, lungs and the heart. Quantitative measurements of the radioactivity from all organs (Fig. S12†) indicated the biodistribution to be predominantly in the liver (92 ± 10% of the administered dose) and spleen (5 ± 1%) with trace distributions, within experimental error, in the brain and kidneys.

Conclusions

To summarize, targeted, tomographic and quantitative cancer diagnosis using MPI requires optimized NPs with a tuned crystalline structure and phase purity to enhance the signal intensity and resolution. In addition, the surface of these optimized NPs should be properly functionalized to improve their blood circulation time, tumor targeting and retention. Here, using a general surface functionalization platform, we conjugated a targeting glycoprotein to the NP surface, in order to increase the uptake of the NPs by a brain tumor xenograft to levels greater than the sensitivity of current MPI scanners. Our functionalized platform, with glioma-targeting lactoferrin, conjugated to the PMAO-PEG surface of the optimized MPI contrast agents, enhanced uptake by tumors. Magnetic targeting further improved the tumor uptake of the NPs. High contrast agent mass sensitivity and fast image processing of NIRF, in combination with MPI analyses enabled us to monitor the NP uptake by tumors and perform preliminary feasibility testing of tumor targeted MPI. Multimodal MPI/CT/X-ray imaging enabled us to generate 2D and 3D tomographic and positive contrast images of these cancers in mouse models with very high signal-to-noise ratios (SNR). In addition, radiolabeling of these optimized MPI contrast agents by ^{67}Ga-NOTA, followed by highly sensitive and quantitative SPECT/CT imaging, confirmed that these NPs had no discernable renal clearance, since their hydrodynamic sizes (100–110 nm) were much larger than the endothelial fenestrae in kidneys (5–15 nm). Note that the hydrodynamic size and surface charge of the NPs did not have a noticeable change after their radiolabeling. Therefore, their *in vivo* behavior should not change after radiolabeling, since these are the major factors determining NP biodistribution and pharmacokinetics.[27] Previous studies have shown that lactoferrin molecules can pass the blood brain barrier (BBB) through a receptor-mediated transcytosis mechanism.[30] Therefore, future investigations using intracranially implanted brain tumor xenografts are required to validate the facilitated BBB transport of these lactoferrin conjugated NPs. These proof of concept results hold promise for the safe clinical translation of our MPI contrast agents. Our flexible PMAO-PEG coating platform further provides opportunities for various conjugation strategies, ideal for multimodal MPI/CT/NIRF/MRI/CT/SPECT imaging, and each one with distinct advantages.

Experimental

Synthesis of the maleimide functionalized PMAO-PEG copolymers

Maleimide functionalized PMAO-PEG (Fig. 2a) was synthesized by amide bond formation between heterobifunctional maleimide-poly(ethylene glycol)-amine (Mal-PEG, M_n ~ 7.5 kDa), methoxy-poly(ethylene glycol)-amine (m-PEG, M_n ~ 20 kDa), and poly(maleic anhydride-*alt*-1-octadecene) (PMAO, M_n ~ 30–50 kDa). Briefly, 1.75 μmol (70 mg) PMAO and 4 μmol (30 mg) Mal-PEG were dissolved in 3 mL dichloromethane (DCM) followed by the addition of 10 μL triethylamine. This mixture was protected from light and allowed to react for 4 hours, and then 68 μmol (1360 mg) m-PEG, 2 mL DCM, and

50 μL triethylamine were added. The mixture was again protected from light and allowed to react. After 48 hours, the polymer was dried by rotary evaporation, dissolved in deionized (DI) water, and purified by membrane dialysis with a molecular weight cut-off of 50 kDa. An increase in molecular weight was confirmed by Gel Permeation Chromatography (GPC).

Synthesis and phase transfer of the optimized MPI contrast agents

Monodisperse hydrophobic NPs ($d_C \sim 27$ nm) were synthesized by modification of a method we reported previously.[22,23] The as-synthesized NPs were dispersed in a 5 mL mixture of hexanes and ethyl acetate (1 : 1) by sonication (~30 s) and then separated by using a strong magnet. This step was repeated once with a mixture of hexanes and ethyl acetate (1 : 2), and three times with a mixture of hexane and acetone (1 : 1). The purified NPs (~10 mg) were then dried under vacuum and re-dispersed in 10 mL chloroform by sonication (~3 min). 150 mg of the maleimide functionalized PMAO-PEG co-polymer was added to the NPs and sonicated (~3 min), followed by overnight stirring using a small magnetic stir bar. Rotary evaporation was used to remove chloroform and then 10 mL DI water was added to the dried mixture of NPs and the polymer, followed by 2 hours of sonication to re-disperse the NPs. The water dispersed PMAO-PEG coated NPs (Fig. 2b) were concentrated by using a centrifugation filter with a molecular weight cut-off of 50 kDa.

Conjugation of lactoferrin to NPs

Lactoferrin was thiolated by modification of a method reported previously.[31] First, we dissolved 1 mg of lactoferrin in 1 mL PBS. Then, 50 μg of 2-iminothiolane (also called Traut's reagent) was mixed with the lactoferrin solution for 1.5 h in the dark at room temperature, followed by purification using Amicon® ultra-centrifugal filters (MWCO: 30 kDa). The final NPs were re-dispersed in the same amount of PBS. The thiolated lactoferrin was then added to the NP solution, wrapped in aluminum foil and placed on a shaker at room temperature overnight. Then, the lactoferrin conjugated NPs were purified using PD-10 columns equilibrated with sodium bicarbonate (pH ~ 8–8.5) buffer. Five milligrams of Cy5.5-NHS NIRF molecules (emission and excitation wavelengths ~673 and 707 nm, respectively, and fluorescence quantum yield ~0.2) were dissolved in 0.5 mL of DMSO and then 100 μL of this solution was added to each 1 mg of lactoferrin conjugated NPs. The mixture was wrapped in aluminum foil and placed on a shaker for 2 hours. Finally, the NPs were purified using Amicon centrifuge vials (MWCO: 30 kDa) to remove the un-reacted Cy5.5 molecules from the NP solution and redispersed in PBS solution for animal studies. We also synthesized a separate batch without any lactoferrin for comparison. To do this, we added 100 mg NH_2-PEG-SH (3.4 kDa) to the NP solution (1 mg Fe), sonicated the mixture for 15 min to make sure the entire polymer was dissolved and then wrapped the mixture in aluminum foil and placed it on a shaker overnight. The thiol groups of the PEG reacted with the maleimide groups on the surface of the NPs and their other amine terminating tails were used for Cy5.5 conjugation, as described above.

Radiolabeling of the NPs

For ligand modification and ^{67}Ga-radiolabeling, nanoparticles were modified with the chelator *p*-SCN-bz-NOTA (Macrocyclics, USA) and then radiolabeled with gallium-67 (^{67}Ga, $t_{1/2}$ = 78.3 h) (Fig. S1†). For this purpose, 800 μL of the particles were diluted with $NaHCO_3$ (800 μl, 0.1 N) and incubated with 0.8 mg of *p*-SCN-bz-NOTA solution at 19 °C overnight. The particles were concentrated using Amicon® ultra-centrifugal filters (MWCO: 30 kDa), washed twice and re-suspended in 1 mL PBS. NOTA was bound to the amine groups on the surface of NPs through a thiourea bond. NPs were radiolabeled by adding $^{67}GaCl_3$ (5.3 mCi) to the suspension and incubating at room temperature for 30 min with mixing, followed by Amicon concentration and washing twice with PBS (92% labeling efficiency). The radiolabeled particles (^{67}Ga-NP) were dispersed in 500 μl PBS for the biodistribution studies. The hydrodynamic size and zeta potential of the labeled nanoparticles were 121 nm (PDI: 0.201) and −36 mV.

NP characterization

Transmission electron microscopy (TEM, FEI Tecnai™ G2 F20, 200 keV), equipped with a Gatan CCD camera, was used to analyze the size and morphology of the synthesized NPs. Magnetization behavior (*m*–*H*) of the NPs (~150 μg of NP solution in 100 μL polycarbonate capsules) was studied using a vibrating sample magnetometer (VSM, Lakeshore). Dynamic light scattering (DLS, Zetasizer Nano, Malvern Instruments) was used to measure the hydrodynamic size of the PEG coated NPs. An Inductively Coupled Plasma Optical Emission Spectrophotometer (ICP-OES, PerkinElmer Optima 8300) was used to determine the iron concentration in each NP solution.

We also used a custom-built magnetic particle spectrometer (MPS) with a sinusoidal excitation field of 18.6 $mT\mu_0^{-1}$ (peak–peak, f_0 = 25 kHz) to evaluate the MPI performance (*i.e.*, d*m*/d*H*) of the synthesized NPs.[20,32] The data processing method for calculating d*m*/d*H* graphs from the induced voltage in receiving coils of the MPS was reported earlier.[20] All d*m*/d*H* plots obtained from the MPS were normalized to one in order to compare their FWHM, which is a good indicator, to first order, of the potential spatial resolution in an MPI scanner.

Preparation of the mice with C6 brain cancer xenografts

Athymic female CD-1 nude mice (12 mice, 25–30 g, 12 weeks old, Charles River Laboratories) were used as models for our tumor uptake studies, based on the animal use protocols reviewed and approved by the Institutional Animal Care and Use Committee (IACUC) of the University of Washington. Mice were housed in ventilated cages with specific pathogen free facilities and provided free access to food and water. Animals were not maintained with any specific diet such as foods with low autofluorescence signals. To generate the tumor xenografts required for this investigation, we used subcutaneous injection

of C6 rat glioma cells (ATCC® CCL-107™, 10^6 cells in 100 μL of DMEM–10% FBS cell culture media and 100 μL of Matrigel) into the right flanks of the mice. The tumor growth was monitored daily and nanoparticles were injected after about 3–4 weeks.[25]

NP administration

Mice were injected, under 2–3% isoflurane anesthesia, *via* the tail veins with 200 μL of a sterile filtered 1 g Fe per L iron oxide nanoparticles suspended in phosphate buffered saline (1×, PBS). To aid in NP targeting two axially connected small neodymium rare earth magnetic discs (3/8 × 1/8 inches, N48, magnetic field strength ~3.900 gauss, at an angle of 0° from the vertical axis) were placed on the skin adjacent to the tumors and fixed in place for about 2 h using sterile wound tape, based on the results reported by Cole *et al.*[33] We compared the targeting results with and without using an external magnet. Control animals had no magnet taped to the tumor.

In vivo and *ex vivo* imaging of the excised tumors (IVIS and MPS)

Before the injections, and 1 and 2 hours of post-injection, mice were monitored using an IVIS fluorescence imaging system (Caliper Life Sciences, USA, equipped with the Living Image software package) to evaluate nanoparticle uptake in the tumor, liver, spleen, kidneys, lungs, brain and heart. During the nanoparticle injections and imaging steps, mice were maintained under 2–3% isoflurane anesthesia. Anesthetized animals were euthanized using cervical dislocation after *in vivo* imaging and the tumors were excised for fluorescence imaging and MPS measurements. We used 3 mice for each condition to determine the targeting efficiency using whole body and xenograft IVIS imaging and MPS.

MPI/CT/X-ray imaging

MPI images of the mice were acquired with the projection Field Free Line (FFL) Momentum MPI scanner (Magnetic Insight Co., Fig. S2†), operating with a magnetic field gradient strength of 6 × 6 T m^{-1}. Mice were translated along the *z*-axis of the scanner using a single-axis translation stage, with a field-free line along the *y*-axis and an excitation field (45 kHz, 20 mT peak amplitude) along the *z*-axis. The overlap fraction and harmonic bandwidth were 90% and 1000 kHz, respectively. Note that the overlap fraction represents the path traversed by the FFL when generating the image and a higher overlap fraction generally improves the SNR by increased averaging. Images were captured with a field of view (FOV) of 6 cm × 8 cm and an acquisition time of 10 seconds per projection (number of projections = 55), plus 30 seconds for automatic set up of the magnets and about 35 minutes for image reconstruction (total time ~40 min). CT scans were acquired for anatomical references, using a MicroCT (TriFoil Imaging CT120) scanner, with about 10 minutes acquisition time and 100 μm isotropic resolution. Fiducial points (2.5 μL of NPs with a concentration of 500 μg Fe per mL, sealed in PTFE tubing (Cole-Parmer, 1/32″ and 1/16″ internal and external diameters)) were used for 2D and 3D registration of the MPI images with CT scans and as standards for the quantification of the NPs in tissues. VivoQuant software was used for 2D and 3D image reconstruction, registration and NP quantification.

SPECT/CT imaging

For biodistribution studies using SPECT/CT imaging, three female C57Bl6 mice (Charles River Laboratories) were injected each ^{67}Ga-NP (1 mCi, 120 μL; ^{67}Ga (γ: 93, 185, 300, 393 keV, 100% EC)) *via* the tail vein. The animals were scanned individually using a MILabs VECTor/CT SPECT/CT scanner (imaging protocol approved by the University of British Columbia Animal Care Committee according to the guidelines set out by the Canadian Council on Animal Care) immediately and at 4 h post injection, and then euthanized. Following each SPECT acquisition, a whole body CT scan was performed to obtain anatomical information and both images were registered. For quantitative analysis, SPECT data were reconstructed with the ordered subset expectation maximization algorithm (OS-EM) using 6 iterations of 16 subsets and 0.4 mm^3 voxel size. All organs were then counted for radioactivity.

Conflicts of interest

None of the authors have any conflicts of interest in this publications.

Acknowledgements

This work was supported by NIH grants 1RO1EB013689-01 (National Institute of Biomedical Imaging and Bioengineering, NIBIB), 1R41EB013520-01 and 2R42EB013520-02A1. The SPECT/CT imaging protocol was approved by the UBC's ACC, according to the CCAC guidelines. Part of this work was conducted at the University of Washington Molecular Analysis Facility (MAF), a member of the NSF National Nanotechnology Infrastructure Network (NNIN). HA, ET and KMK also acknowledge helpful discussions with Dr S. Kemp, Dr A. P. Khandhar, and Dr R. M. Ferguson. HA acknowledges supports provided by Stanford Cancer Imaging Training (T32) program NIH U01 CA187947. The authors thank Magnetic Insight Inc. for valuable input and support for generation of MPI results. The authors also appreciate Dr Chirag Patel for helpful discussions regarding statistical analyses.

References

1 M. Graeser, T. Knopp, P. Szwargulski, T. Friedrich, A. v. Gladiss, M. Kaul, K. M. Krishnan, H. Ittrich, G. Adam and T. M. Buzug, *Sci. Rep.*, 2017, 7, 6872.

2 R. M. Ferguson, A. P. Khandhar, S. J. Kemp, H. Arami, E. U. Saritas, L. R. Croft, J. Konkle, P. W. Goodwill, A. Halkola, J. Rahmer, J. Borgert, S. M. Conolly and K. M. Krishnan, *IEEE Trans. Med. Imaging*, 2015, **34**, 1077–1084.

3 B. Gleich and J. Weizenecker, *Nature*, 2005, **435**, 1214–1217.
4 K. M. Krishnan, *Fundamentals and Applications of Magnetic Materials*, Oxford University Press, Oxford, 2016.
5 R. M. Ferguson, A. P. Khandhar, H. Arami, L. Hua, O. Hovorka and K. M. Krishnan, *Biomed. Eng.*, 2013, **58**, 493–507.
6 P. W. Goodwill, E. U. Saritas, L. R. Croft, T. N. Kim, K. M. Krishnan, D. V. Schaffer and S. M. Conolly, *Adv. Mater.*, 2012, **24**, 3870–3877.
7 K. M. Krishnan, *IEEE Trans. Magn.*, 2010, **46**, 2523–2558.
8 E. U. Saritas, P. W. Goodwill, L. R. Croft, J. J. Konkle, K. Lu, B. Zheng and S. M. Conolly, *J. Magn. Reson.*, 2013, **229**, 116–126.
9 M. H. Pablico-Lansigan, S. F. Situ and A. C. S. Samia, *Nanoscale*, 2013, **5**, 4040–4055.
10 A. P. Khandhar, R. M. Ferguson, H. Arami and K. M. Krishnan, *Biomaterials*, 2013, **34**, 3837–3845.
11 A. P. Khandhar, P. Keselman, S. J. Kemp, R. M. Ferguson, P. W. Goodwill, S. Conolly and K. M. Krishnan, *Nanoscale*, 2017, **9**, 1299–1306.
12 E. Yu, M. Bishop, B. Zheng, R. Ferguson, A. Khandhar, S. Kemp, K. M. Krishnan, P. W. Goodwill and S. M. Conolly, *Nano Lett.*, 2017, **17**, 1648–1654.
13 R. Orendorff, A. J. Peck, B. Zheng, S. N. Shirazi, R. M. Ferguson, A. P. Khandhar, S. J. Kemp, P. Goodwill, K. M. Krishnan, G. A. Brooks, D. Kaufer and S. Conolly, *Phys. Med. Biol.*, 2017, **62**, 3501.
14 X. Y. Zhou, K. E. Jeffris, E. Yu, B. Zheng, P. W. Goodwill, P. Nahid and S. M. Conolly, *Phys. Med. Biol.*, 2017, **62**, 3510.
15 B. Zheng, P. Marc, E. Yu, B. Gunel, K. Lu, T. Vazin, D. V. Schaffer, P. W. Goodwill and S. M. Conolly, *Theranostics*, 2016, **6**, 291–301.
16 B. Zheng, K. Lu, J. J. Konkle, D. W. Hensley, P. Keselman, R. D. Orendorff, Z. W. Tay, E. Yu, X. Y. Zhou, M. Bishop, B. Gunel, L. Taylor, R. M. Ferguson, A. P. Khandhar, S. J. Kemp, K. M. Krishnan, P. W. Goodwill and S. M. Conolly, *Design and Applications of Nanoparticles in Biomedical Imaging*, Springer, 2017, pp. 69–93.
17 A. Tomitaka, H. Arami, S. Gandhi and K. M. Krishnan, *Nanoscale*, 2015, **7**, 16890–16898.
18 R. M. Ferguson, A. Khandhar, H. Arami, L. Hua, O. Hovorka and K. M. Krishnan, *Biomed. Eng.*, 2013, 1–15.
19 P. W. Goodwill and S. M. Conolly, *IEEE Trans. Med. Imaging*, 2011, **30**, 1581–1590.
20 H. Arami, R. M. Ferguson, A. P. Khandhar and K. M. Krishnan, *Med. Phys.*, 2013, **40**, 071904.
21 H. Arami and K. M. Krishnan, *J. Appl. Phys.*, 2014, **115**, 17B306.
22 S. J. Kemp, R. M. Ferguson, A. P. Khandhar and K. M. Krishnan, *RSC Adv.*, 2016, **6**, 77452–77464.
23 R. Hufschmid, H. Arami, R. M. Ferguson, M. Gonzales, E. Teeman, L. N. Brush, N. D. Browning and K. M. Krishnan, *Nanoscale*, 2015, **7**, 11142–11154.
24 H. Arami and K. M. Krishnan, *IEEE Trans. Magn.*, 2013, **49**, 3500–3503.
25 F. M. Kievit, O. Veiseh, N. Bhattarai, C. Fang, J. W. Gunn, D. Lee, R. G. Ellenbogen, J. M. Olson and M. Q. Zhang, *Adv. Funct. Mater.*, 2009, **19**, 2244–2251.
26 H. Arami, A. P. Khandhar, A. Tomitaka, E. Yu, P. W. Goodwill, S. M. Conolly and K. M. Krishnan, *Biomaterials*, 2015, **52**, 251–261.
27 H. Arami, A. Khandhar, D. Liggitt and K. M. Krishnan, *Chem. Soc. Rev.*, 2015, **44**, 8576–8607.
28 K. Saatchi, S. E. Tod, D. Leung, K. E. Nicholson, I. Andreu, C. Buchwalder, V. Schmitt, U. O. Häfeli and S. L. Gray, *Nanomedicine*, 2017, **13**, 559–568.
29 R. Misri, K. Saatchi and U. O. Hafeli, *Nanomedicine*, 2012, **7**, 719–733.
30 S. Kumari, S. M. Ahsan, J. M. Kumar, A. K. Kondapi and N. M. Rao, *Sci. Rep.*, 2017, **7**, 6602.
31 F. M. Kievit, Z. R. Stephen, O. Veiseh, H. Arami, T. Z. Wang, V. P. Lai, J. O. Park, R. G. Ellenbogen, M. L. Disis and M. Q. Zhang, *ACS Nano*, 2012, **6**, 2591–2601.
32 R. M. Ferguson, A. P. Khandhar and K. M. Krishnan, *J. Appl. Phys.*, 2012, **111**, 07B318.
33 A. J. Cole, A. E. David, J. X. Wang, C. J. Galban, H. L. Hill and V. C. Yang, *Biomaterials*, 2011, **32**, 2183–2193.